

# 1 Direct current microplasma formation around microstructure arrays

2 Yangyang Fu,<sup>1</sup> Huihui Wang,<sup>2</sup> Bocong Zheng,<sup>3</sup> Peng Zhang,<sup>4</sup> Qi Hua Fan,<sup>4,3,5</sup> Xinxin Wang,<sup>1</sup> and John P. Verboncoeur<sup>6,4</sup>

3 <sup>1</sup>Department of Electrical Engineering, Tsinghua University, Beijing, 100084, China

4 <sup>2</sup>EMD Performance Materials, Tempe, Arizona, 85224, United States of America

5 <sup>3</sup>Fraunhofer Center for Coatings and Diamond Technologies,  
Michigan State University, East Lansing, Michigan 48824, United States of America

6 <sup>4</sup>Department of Electrical and Computer Engineering, Michigan State University,  
East Lansing, Michigan 48824, United States of America

7 <sup>5</sup>Department of Chemical Engineering and Materials Science,  
Michigan State University, East Lansing, Michigan 48824, United States of America

8 <sup>6</sup>Department of Computational Mathematics, Science and Engineering,  
Michigan State University, East Lansing, Michigan 48824, United States of America

9 (Dated: April 4, 2021; Authors to whom correspondence should be addressed: fuyangyang@tsinghua.edu.cn, bzheng@fraunhofer.org)

10 We demonstrate the formation and transition behaviors of a microplasma around microstructure arrays at different  
11 gas pressures via two-dimensional particle-in-cell/Monte Carlo collision (2d3v) simulations. It is found  
12 that the microdischarge occurs outside the cathode microcavities at the lowest pressure, and starts penetrating  
13 the microcavities with a curved sheath edge as the pressure increases. At high pressure, coupled periodic micro-  
14 hollow cathode discharges (MHCDs) are formed inside the microcavities. Further increasing the gas pressure  
15 results in the disappearance of the MHCDs, and the dominant discharge shifts outside of the microcavity, locat-  
16 ing above the protrusion tips. The effect of the space charge shielding on the discharge and the conditions for  
17 MHCD formation are discussed. The macroscopic discharge parameters scaling with the gas pressure and the  
18 electron kinetics are also examined. The results are helpful for deeply understanding the microplasma forma-  
19 tion with nonplanar electrodes, which inform the scaling, design, and optimization of microplasma array devices  
20 across a wide range of pressure regimes in practical applications.

21 Microplasmas have received growing attention during the  
22 past decades due to their potential for a wide range of appli-  
23 cations, such as photonic crystals [1], excimer sources [2],  
24 analytical chemistry [3], thin film synthesis [4], and plasma  
25 medicine [5]. Various discharge configurations have been uti-  
26 lized for the generation of microplasmas, including dielec-  
27 tric barrier discharges [6], microplasma jets [7], microhol-  
28 low cathode discharges (MHCDs) [8], and others [9–13]. Mi-  
29 croplasma devices with independently addressable microcav-  
30 ities for light sources and control electronics have been com-  
31 prehensively studied by Eden’s group [14–16]. Hopwood *et*  
32 *al.* studied the ignition of microwave microplasma with mi-  
33 crostrip resonators and presented the scale-up microplasma  
34 using an array concept [17, 18]. Kushner’s group investigated  
35 the microplasma array for controlling the propagation of elec-  
36 tromagnetic waves and found that the transmitted power can  
37 be tuned by the spatial distribution of microplasma cells [19].  
38 More recently, a microdischarge array device with dielectric  
39 holes was fabricated as an ozone generator with flexible per-  
40 formance and high efficiency achieved [20]. With recent ad-  
41 vances in microfabrication technologies, the configurations of  
42 microplasma devices are becoming increasingly diverse.

43 Although many applications of microplasma devices have  
44 been developed, diagnosing the microdischarges is still rather  
45 challenging due to the significantly reduced gap dimensions.  
46 The conventional probe measurement (e.g., Langmuir probe  
47 [21]) and the spectroscopy technique are hardly possible for  
48 precise spatially resolved diagnosis. Numerical simulations  
49 based on hydrodynamic and fully kinetic models are power-  
50 ful tools and widely utilized to understand the fundamental  
51 mechanisms of the microplasmas [22–27]. However, many of  
52 the simulation studies were carried out for planar electrodes

53 or focusing on a single unit between nonplanar electrodes for  
54 simplicity. The simulation with ideal planar electrodes can-  
55 not characterize the effect of the surface morphology on the  
56 discharge. For the simulation with a single unit between non-  
57 planar electrodes, on one hand, if the periodic boundary con-  
58 dition is used, the plasma is assumed to be duplicated peri-  
59 odically in the radial direction and the sidewall effect is just  
60 ignored; on the other hand, if the boundary in a single unit  
61 is treated as a sidewall, the microplasma will be largely af-  
62 fected by the side wall since the sheath region can occupy a  
63 considerable part of the microgap. Therefore, the simplified  
64 simulation setups may not fully reflect the practical conditions  
65 which typically have many structural units and a sealed side-  
66 wall. Our previous studies have characterized the effect of the  
67 nonplanar electrode surface morphology (e.g., hemispherical  
68 cathode protrusion) on microgap breakdown [28–30]. Never-  
69 theless, the investigation of microdischarge around nonplanar  
70 perturbations is far from complete, and the physics of how  
71 a microplasma responds to a multidimensional surface mor-  
72 phology is still not fully understood.

73 In this work, we demonstrate the generation and character-  
74 istics of a microplasma around the microstructure arrays on  
75 the cathode surface in a microgap. The transition behaviors  
76 of the microdischarge at different pressures are characterized  
77 using two-dimensional particle-in-cell/Monte Carlo collision  
78 (PIC/MCC, 2d3v) simulations. It is found that the discharges  
79 are above the microcavity at lower pressure and localized to  
80 the microstructures at higher pressure. The macroscopic dis-  
81 charge parameter scaling to the gas pressure and the electron  
82 kinetics are presented. The results from this work provide  
83 more comprehensive understanding and better optimization  
84 of the operation of microplasma array devices with structured

78 electrodes in practical applications.

79 The schematic slice of the microgap in Cartesian geometry  
 80 ( $xy$ ) is shown in Fig. 1. The microgap consists of one planar  
 81 anode and a structured cathode with an array of microcavities.  
 82 A direct-current voltage  $V_{dc}$  is applied to the anode through a  
 83 ballast resistor  $R_b$  while the cathode is grounded.  $d_1$  and  $d_2$   
 84 are the shortest and longest gap distance;  $w_1$  and  $w_2$  are the  
 85 protrusion width and cavity width;  $w_3$  is the distance between  
 86 the outer cavity and the cathode edge. In this work, the dis-  
 87 charge conditions are  $V_{dc} = 800$  V,  $R_b = 100$  k $\Omega$ ,  $d_1 = 150$   $\mu\text{m}$ ,  
 88  $d_2 = 200$   $\mu\text{m}$ ,  $w_1 = 50$   $\mu\text{m}$ ,  $w_2 = 50$   $\mu\text{m}$ , and  $w_3 = 100$   $\mu\text{m}$ .  
 89 The microgap in the  $z$ -direction is ideally uniform and since  
 90 the external circuit is considered, the depth is set to 100  $\mu\text{m}$ , in  
 91 order to determine the discharge conditions in the modeling.  
 92 The ion-impact secondary electron emission from the cathode  
 93 is considered and the effective secondary electron emission  
 94 coefficient is 0.1 [22]. A Neumann boundary condition is used  
 95 at the inner dielectric sidewall with surface charge accumula-  
 96 tion and  $\partial\phi/\partial x = 0$  for the electric potential is used at  $x =$   
 97 0 and 550  $\mu\text{m}$ . The simulations are performed with argon at  
 98 300 K, accounting for three electron-neutral collisions (elas-  
 99 tic, excitation, and ionization scattering) and two ion-neutral  
 100 collisions (isotropic and backward scattering) [31].

101 The simulations are conducted using a custom-developed  
 102 two-dimensional PIC/MCC model (Astra code [32]) with an  
 103 implicit algorithm. The gas pressure  $p$  varies from 10 Torr  
 104 to 200 Torr. For the cases with  $p > 50$  Torr, the cell sizes  
 105 are  $\Delta x = \Delta y = 1$   $\mu\text{m}$  and the time step is  $\Delta t = 0.1$  ps. Since  
 106 implicit algorithm and energy conserving scheme used here  
 107 alleviate the constraints of the space and time steps,  $\Delta x =$   
 108  $\Delta y = 2$   $\mu\text{m}$  and  $\Delta t = 0.2$  ps are used to accelerate the simu-  
 109 lation at lower pressure, which generally takes a longer phys-  
 110 ical time to reach a steady state. The results presented in the  
 111 following are from the simulations at the steady state. The  
 112 number of superparticles in our simulations is on an order of  
 113 one million and case dependent. The maximum number of  
 114 superparticles per cell (not the averaged number) is around  
 115 100 at low pressures and about 150  $\sim$  300 at higher pres-  
 116 sures (with smaller discharge regions). Although the colli-  
 117 sion frequency approaches the plasma frequency for higher  
 118 pressure cases (e.g., with a larger  $pd$  value), under which  
 119 conditions strictly converged simulations may not be easily  
 120 obtained with reasonable computational cost, the phenomena  
 121 occurring predominantly in the sheath region, such as the dis-  
 122 charge impedance and the power deposition, can still be ac-  
 123 curately captured [33, 34]. The same discharge characteris-  
 124 tics were also observed in the simulations even using fewer  
 125 superparticles. Our simulations combined with the implicit  
 126 algorithm and energy conservation scheme can substantially  
 127 alleviate the self-heating [32, 35], which ensures the fidelity  
 128 of the simulation results.

129 The spatial distributions of the electron density are shown  
 130 in Fig. 2, demonstrating the transition behaviors of the mi-  
 131 crodischarge at different pressures. The gas pressure in  
 132 Figs. 2(a)–2(f) is 10 Torr, 20 Torr, 50 Torr, 100 Torr, 150  
 133 Torr, and 200 Torr, respectively. In Fig. 2(a), the electron  
 134 density is concentrated above the structured cathode and rel-  
 135 atively uniform in the center. The discharge is less perturbed

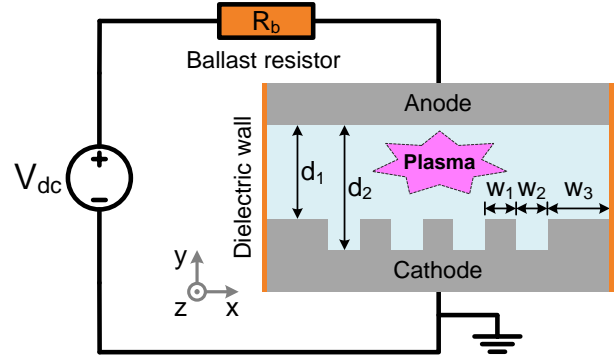


Figure 1. Schematic of the microgap with the structured cathode and dielectric sidewall in Cartesian geometry ( $xy$ ).  $V_{dc}$  is the applied voltage and  $R_b$  is the ballast resistor;  $d_1$  and  $d_2$  are the shortest and longest gap distance;  $w_1$  and  $w_2$  are the protrusion width and cavity width;  $w_3$  is the distance between the outer cavity and the cathode edge. In this work,  $V_{dc} = 800$  V,  $R_b = 100$  k $\Omega$ ,  $d_1 = 150$   $\mu\text{m}$ ,  $d_2 = 200$   $\mu\text{m}$ ,  $w_1 = 50$   $\mu\text{m}$ ,  $w_2 = 50$   $\mu\text{m}$ , and  $w_3 = 100$   $\mu\text{m}$ .

136 by the irregularity of the cathode. Since the sheath width  $d_s$   
 137 is larger than the microcavity dimension ( $d_s > w_2 = 50$   $\mu\text{m}$   
 138 at 10 Torr), the perturbation of the nonplanar structures is  
 139 screened because of the space charge shielding effect. The  
 140 density profile is smoothed away from the cathode and the  
 141 sheath edge is relatively flat. In Fig. 2(b), the plasma sheath  
 142 becomes narrower at a higher pressure and the perturbation  
 143 of the electrode irregularity is observed. There are multiple  
 144 electron density peaks right above the cathode microcavities  
 145 with the maximum electron density increased. The cathode  
 146 sheath edge is curved, which demonstrates the impact of the  
 147 nonplanar electrode. In Fig. 2(c), the sheath edge becomes  
 148 more curved and the maximum electron density is further in-  
 149 creased; the electron density peaks start penetrating the micro-  
 150 cavities. At 100 Torr, the MHCDs are formed (see Fig. 2(d)),  
 151 and the electron density is significantly enhanced, reaching an  
 152 order of  $10^{21}$  m $^{-3}$ . Meanwhile, the negative glow region out-  
 153 side the cavity becomes less pronounced. In Fig. 2(e), at 150  
 154 Torr the maximum electron density slightly decreases while  
 155 the discharge is still in the MHCD mode. However, further  
 156 increasing the gas pressure results in the disappearance of the  
 157 MHCDs (see Fig. 2(f)). At 200 Torr, the dominant discharge  
 158 region shifts outside the cathode microcavities and the max-  
 159 imum electron density is reduced. The sheath width and the  
 160 negative glow regions are obviously constricted due to the suf-  
 161 ficiently high pressure. The opposite negative glow regions,  
 162 which remain inside the microcavity, are separated without  
 163 forming the typical MHCD. Note that here the sidewall is rel-  
 164 atively far from the center and thus its effect on the plasma is  
 165 less pronounced than the simulation using a single structure  
 166 unit, in which the sheath width could be more comparable to  
 167 the size of microplasma.

168 Figure 3 shows the spatial distributions of the electric po-  
 169 tential, corresponding to the cases in Fig. 2. The contour  
 170 (equipotential) line corresponds to  $0.9\phi_{max}$  ( $\phi_{max}$  is the max-  
 171 imum electric potential) in each case. In Figs. 3(a)–3(c), the  
 172 dominant potential drop occurs outside of the microcavities;

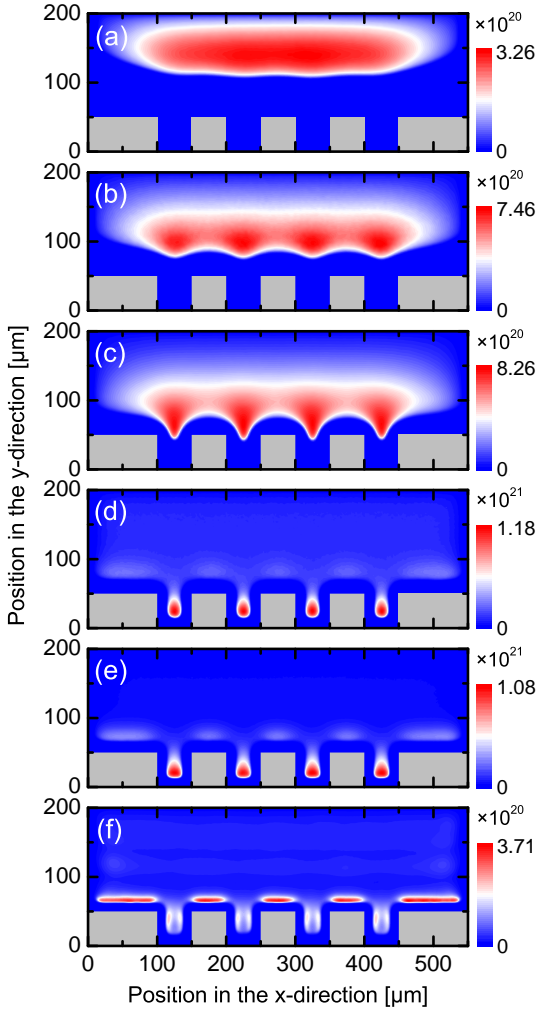


Figure 2. Spatial distributions of the electron density  $n_e$  [unit in  $\text{m}^{-3}$ ] at (a) 10 Torr, (b) 20 Torr, (c) 50 Torr, (d) 100 Torr, (e) 150 Torr, and (f) 200 Torr, respectively. The microplasma at 100 Torr shows the highest electron density inside the microcavity.

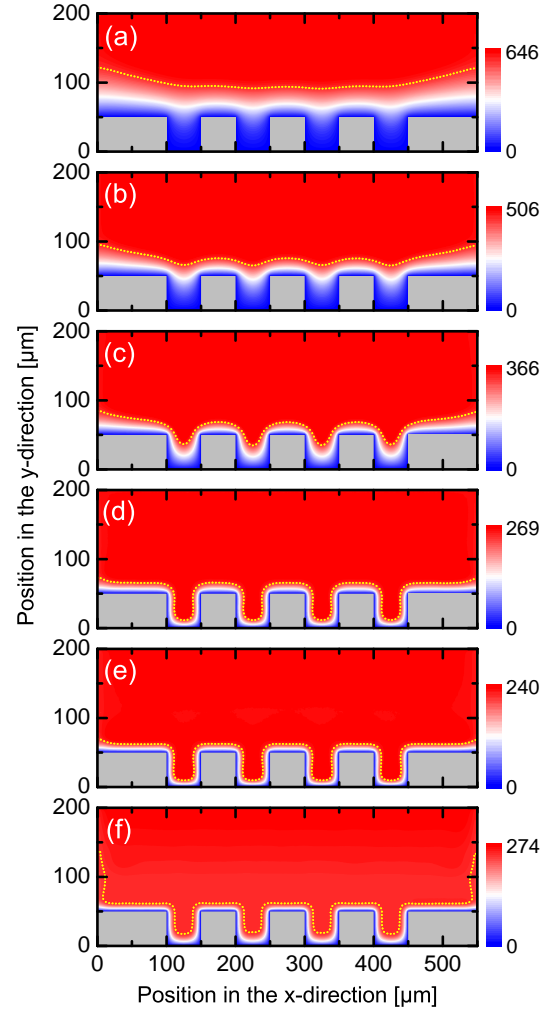


Figure 3. Spatial distributions of the electric potential  $\phi$  [unit in V] at (a) 10 Torr, (b) 20 Torr, (c) 50 Torr, (d) 100 Torr, (e) 150 Torr, and (f) 200 Torr, respectively. The contour line corresponds to  $0.9\phi_{max}$  ( $\phi_{max}$  is the maximum electric potential) in each case.

as the gas pressure increases, the equipotential line transits from flat to curved contour, which is also consistent with the gradually curved sheath edge (see Figs. 2(a)–2(c)). In Figs. 3(d)–3(f), at higher pressures the cathode fall layers are generally smaller and most of the microgap domain, including the microcavity, is equipotential. The  $0.9\phi_{max}$  potential drop width is very narrow for discharges in the MHCD mode (see Figs. 3(d) and 3(e)). However, at 200 Torr the voltage drop from the bottom becomes wider (see Fig. 3(f)) since the discharge does not penetrate sufficiently into the microcavities and the dominant discharge locates above the protrusion tips.

The transition behaviors of the microdischarges are observed in Figs. 2 and 3, which demonstrate the negative glow discharge with gradually curved sheath edge, hollow cathode discharge mode, and glow discharge with constricted cathode fall layer. The electron density is significantly increased when the MHCDs are formed. The microdischarges at high pressure are periodically coupled, forming array microplasmas lo-

calized inside the cathode microstructures. Although the simulation results may change under different discharge conditions, the transition characteristics, according to the similarity law [36], are expected to be generally similar with the same characteristic length, e.g., Knudsen number  $\lambda/L$ , where  $\lambda$  is mean free path and  $L$  is physical dimension [37]. The discharge characteristics are largely determined by the electron mean free path which is expressed as

$$\lambda_e(\varepsilon) = \frac{k_B T_g}{p \sigma_c(\varepsilon)}, \quad (1)$$

where  $k_B$  is the Boltzmann constant,  $T_g$  is the gas temperature,  $p$  is the gas pressure,  $\sigma_c(\varepsilon)$  is the collision cross section [38]. As indicated in Ref. [39], secondary electrons accelerated by the opposite sheaths should collide with neutral particles (at least one collision or ionization) in negative glow to sustain the hollow cathode discharge. Considering the nega-

tive glow size should be larger than  $\lambda_e$ , we have the upper limit  $\lambda_{e,max} = w_2 - 2d_s$ , where  $d_s$  is the sheath width that could also depend on the gas pressure and the discharge current density  $J$ , i.e.,  $d_s = d_s(p, J)$ . The hollow cathode discharge cannot form if  $\lambda_e$  is too large (e.g.,  $\lambda_e > \lambda_{e,max}$ ), or  $\lambda_{e,max} \leq 0$  (e.g.,  $w_2 \leq 2d_s$  in Figs. 2(a)–2(c)) where the negative glow cannot be housed inside the cavity. On the other hand, the MHCD cannot form if  $\lambda_e$  is too small (e.g., at 200 Torr in Fig. 2(f)). Considering the opposite negative glow regions inside the cavity should not be completely separated, we have the lower limit of the electron mean free path  $\lambda_{e,min} = w_2/2 - d_s$ . As shown in Fig. 4(a), the mean free path for electron impact ionization  $\lambda_{iz}$  of secondary electrons is compared to the estimated range  $(\lambda_{e,min}, \lambda_{e,max})$ . The MHCD is observed when  $\lambda_{iz}$  is within or close to the estimated range; otherwise the MHCD cannot form. Therefore, the discharge can only penetrate the microcavity, forming MHCD, at a certain pressure or  $p w_2$  range. Although simplified, it is a straightforward prediction on the relation between the gas pressure and the discharge transition behavior, the validity of which is also confirmed.

According to Refs. [40, 41], the estimated range of  $p w_2$  for MHCD formation in argon should be  $0.026 \sim 10$  Torr · cm [42], the prediction of which, however, does not take the negative glow region into consideration and may not be sufficiently accurate. The experimental results by Schoenbach *et al.* suggest  $p w_2$  ranging from  $0.53 \sim 5$  Torr · cm [8]. Our simulation results suggest the range is about  $0.25 \sim 1$  Torr · cm, which is closer to the experimental results than the rough theoretical estimation. A more appropriate estimation, considering the negative glow width and  $d_s = d_s(p, J)$ , indicates that the upper limit for argon MHCD is  $1.1$  Torr · cm [42], which is almost the same as ours. Note that though rather close, the PIC results and the experiments still have difference, which may be relevant to the different discharge configurations utilized. The coplanar cylindrical holes are used in Ref. [8], while the discharge at higher pressure can still form inside the microcavity, showing a ring structure but without the overlapping of the opposite negative glow regions [43], which may overestimate the upper limit. Other geometrical parameters (e.g.,  $w_1, d_1$ , and  $d_2$ ) may also alter the  $p w_2$  range for the MHCD formation. Our results based on the fully kinetic simulations clearly present the MHCD formation and conditions with the discharge transition behaviors captured, which are beneficial for optimizing microdischarge array devices across different pressure regimes.

The macroscopic discharge parameters scaling with gas pressure is shown in Fig. 4(b). As the pressure increases, the gap voltage  $V_{gap}$  decreases from  $642$  V to the lowest value  $274$  V and then increases. The U-shaped scaling tendency is consistent with previous experimental results of MHCDs (e.g., Yamasaki *et al.* [44]); similar tendencies were also reported by Metel *et al.* [45] and Kolobov *et al.* [46] for classical hollow cathode discharges, which also indicates the validity of the simulation results. Note that  $V_{gap}$  is close to but could be smaller than  $\phi_{max}$  shown in Fig. 3 because of the plasma potential which is slightly positive to the anode [47, 48]. The discharge current  $I_{dis}$  is within the range of  $1.58 \sim 5.63$  mA, while the input power  $P_{in}$  ( $P_{in} = V_{gap} \cdot I_{dis}$ ) varies non-monotonically within the range of  $1.01 \sim 1.58$  W. The charges in the MHCD mode have higher electron densities whereas the power consumption is not the highest, showing an optimized energy efficiency. The discharge power consumption is relatively small (on the level of several Watts) whereas the power density is high (up to hundreds  $\text{kW} \cdot \text{cm}^{-3}$ ) [49], indicating the flexibility in scaling up the array configuration for developing portable plasma equipment.

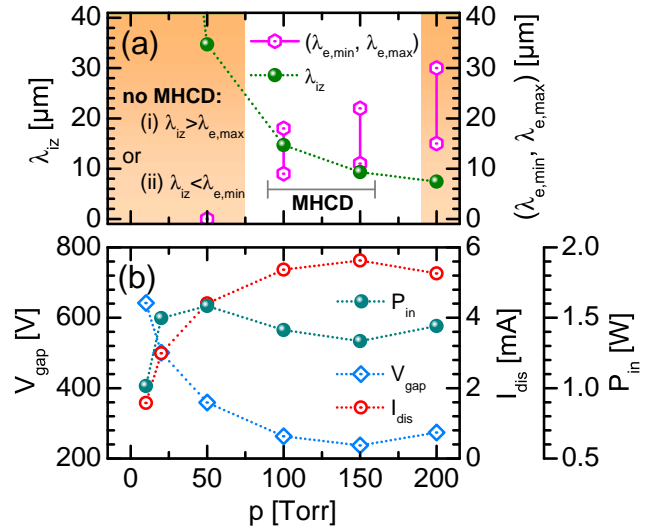


Figure 4. (a) Comparison between the ionization mean free path and the estimated MHCD conditions. (b) Macroscopic discharge parameters scaling with gas pressure.

Figure 5 shows the electron energy probability functions (EEPFs) in full space at different pressures, which are highly non-Maxwellian with boosted high energy tails. As the pressure increases, the boosted high energy tail generally becomes less pronounced, and the maximum electron energy decreases, which corresponds to the maximum sheath voltage drop. When electrons (e.g., secondary electrons) travel across the sheath ballistically, they are accelerated and obtains the full potential energy, converting to kinetic energy [50]. At low pressures, the electrons are more likely traveling ballistically, and maximum electron energy is close to the gap voltage. However, this is not necessarily true at higher pressures when the plasma becomes more collisional. For example, the gap voltage at  $200$  Torr is higher than that at  $150$  Torr, the maximum electron energy still decreases since the electrons may not travel across the sheath ballistically, not obtaining the full potential energy. Note that the high energy tail in the EEPFs is supposed to be little influenced by the numerical relaxation, due to the small physical relaxation time [34].

In summary, we have demonstrated the formation and transition behaviors of microdischarges around microstructure arrays via two-dimensional PIC/MCC simulations. At the lowest pressure, the microplasma is outside the microcavities and the sheath edge is relatively flat due to the space charge shielding effect. As the gas pressure increases, the sheath edge becomes curved and starts penetrating the microcavities on the

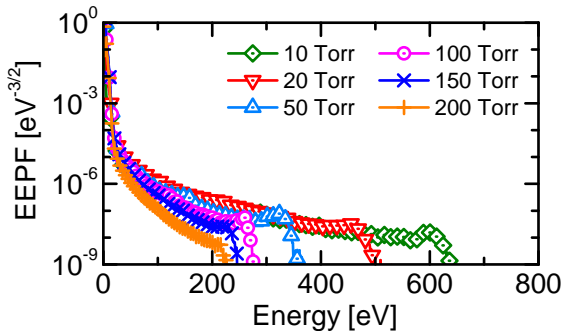


Figure 5. EEPFs in full space at different pressures, which are highly non-Maxwellian with boosted high energy tails.

cathode. At higher pressures, the MHCD is formed inside the microcavity and the electron density is significantly enhanced (order of  $10^{21} \text{ m}^{-3}$ ). Further increasing the gas pressure results in the disappearance of the MHCD and the dominant discharge region shifts to the outside of the microcavities. The condition of the MHCD formation is confirmed with the gradual discharge transition behaviors captured. In all the studied cases, the EEPFs in full space are highly non-Maxwellian and have boosted high energy tails, in which the highest energy corresponds to the maximum sheath potential drop. The microdischarges at high pressures are localized to the cath-

ode microstructures and coupled periodically, which indicates the flexibility in scaling up the microplasma array device toward larger dimension scales. The results from this study are helpful for more comprehensive understanding and better optimization of the operation of microplasma array devices in practical applications. The stability and tunability of the microdischarge interacting with an nonplanar electrode surface morphology across a wider range of the discharge condition parameter regimes and the effect of other electron emission mechanisms will be explored in future work.

## ACKNOWLEDGMENT

The authors are grateful to Professor Hae June Lee for fruitful discussions. This work was supported by the Air Force Office of Scientific Research grant Nos. FA9550-18-1-0062 and FA9550-18-1-0061, the U.S. Department of Energy Office of Fusion Energy Science grant DE-SC0001939, and the National Science Foundation Award Nos. 1917577 and 1724941. Y.F. and H.W. contributed equally to this work.

## DATA AVAILABILITY

The data that support the findings of this study are available from the corresponding author upon reasonable request.

- [1] P. P. Sun, R. Zhang, W. Chen, P. V. Braun, and J. G. Eden, *Appl. Phys. Rev.* **6**, 041406 (2019).
- [2] K. H. Schoenbach, A. El-Habachi, M. M. Moselhy, W. Shi, and R. H. Stark, *Phys. Plasmas* **7**, 2186 (2000).
- [3] D. Janasek, J. Franzke, and A. Manz, *Nature* **442**, 374 (2006).
- [4] H. Kabbara, S. Kasri, O. Brinza, G. Bauville, K. Gazeli, J. Santos Sousa, V. Mille, A. Tallaire, G. Lombardi, and C. Lazaroni, *Appl. Phys. Lett.* **116**, 171902 (2020).
- [5] M. G. Kong, G. Kroesen, G. Morfill, T. Nosenko, T. Shimizu, J. Van Dijk, and J. L. Zimmermann, *New J. Phys.* **11**, 115012 (2009).
- [6] J. Cheng, W. Ding, Y. Zi, Y. Lu, L. Ji, F. Liu, C. Wu, and Z. L. Wang, *Nat. Commun.* **9**, 3733 (2018).
- [7] N. Y. Babaeva and M. J. Kushner, *Plasma Sources Sci. Technol.* **23**, 015007 (2014).
- [8] K. H. Schoenbach, R. Verhappen, T. Tessnow, F. E. Peterkin, and W. W. Byszewski, *Appl. Phys. Lett.* **68**, 13 (1996).
- [9] K. H. Schoenbach and K. Becker, *Eur. Phys. J. D* **70**, 29 (2016).
- [10] K. H. Becker, K. H. Schoenbach, and J. G. Eden, *J. Phys. D* **39**, R55 (2006).
- [11] A. Venkatraman, A. Garg, D. Peroulis, and A. A. Alexeenko, *Appl. Phys. Lett.* **100**, 083503 (2012).
- [12] D. B. Go and A. Venkatraman, *J. Phys. D* **47**, 503001 (2014).
- [13] J. Stephens, A. Fierro, B. Walls, J. Dickens, and A. Neuber, *Appl. Phys. Lett.* **104**, 074105 (2014).
- [14] J. G. Eden and S.-J. Park, *Plasma Phys. Control. Fusion* **47**, B83 (2005).
- [15] S.-J. Park, K.-F. Chen, N. P. Ostrom, and J. G. Eden, *Appl. Phys. Lett.* **86**, 111501 (2005).
- [16] J. G. Eden, S.-J. Park, J. H. Cho, M. H. Kim, T. J. Houlahan, B. Li, E. S. Kim, T. L. Kim, S. K. Lee, K. S. Kim, J. K. Yoon, S. H. Sung, P. Sun, C. M. Herring, and C. J. Wagner, *IEEE Trans. Plasma Sci.* **41**, 661 (2013).
- [17] J. Hopwood, A. R. Hoskinson, and J. Gregório, *Plasma Sources Sci. Technol.* **23**, 064002 (2014).
- [18] Z.-B. Zhang and J. Hopwood, *Appl. Phys. Lett.* **95**, 161502 (2009).
- [19] C. Qu, P. Tian, A. Semnani, and M. J. Kushner, *Plasma Sources Sci. Technol.* **26**, 105006 (2017).
- [20] T. Homola, V. Prukner, P. Hoffer, and M. Šimek, *Plasma Sources Sci. Technol.* **29**, 095014 (2020).
- [21] V. A. Godyak and V. I. Demidov, *J. Phys. D* **44**, 233001 (2011).
- [22] G. Kim, F. Iza, and J. K. Lee, *J. Phys. D* **39**, 4386 (2006).
- [23] M. J. Kushner, *J. Appl. Phys.* **95**, 846 (2004).
- [24] D. Levko and L. L. Raja, *J. Appl. Phys.* **119**, 163303 (2016).
- [25] Y. Fu, P. Zhang, and J. P. Verboncoeur, *Appl. Phys. Lett.* **112**, 254102 (2018).
- [26] F. Iza, J. K. Lee, and M. G. Kong, *Phys. Rev. Lett.* **99**, 075004 (2007).
- [27] A. Semnani, A. Venkatraman, A. A. Alexeenko, and D. Peroulis, *Appl. Phys. Lett.* **103**, 063102 (2013).
- [28] Y. Fu, P. Zhang, and J. P. Verboncoeur, *Appl. Phys. Lett.* **113**, 054102 (2018).
- [29] Y. Fu, J. Krek, P. Zhang, and J. P. Verboncoeur, *IEEE Trans. Plasma Sci.* **47**, 2011 (2018).
- [30] Y. Fu, P. Zhang, J. Krek, and J. P. Verboncoeur, *Appl. Phys. Lett.* **114**, 014102 (2019).
- [31] B. Zheng, Y. Fu, D.-Q. Wen, K. Wang, T. Schuelke, and Q. H. Fan, *J. Phys. D* **53**, 435201 (2020).

- <sup>389</sup> [32] B. Zheng, K. Wang, T. Grotjohn, T. Schuelke, and Q. H. Fan, <sup>409</sup> [43] W. Shi, R. H. Stark, and K. H. Schoenbach, *IEEE Trans.*  
<sup>390</sup> *Plasma Sources Sci. Technol.* **28**, 09LT03 (2019). <sup>410</sup> *Plasma Sci.* **27**, 16 (1999).
- <sup>391</sup> [33] M. M. Turner, *Phys. Plasmas* **13**, 033506 (2006). <sup>411</sup> [44] T. Yamasaki, S. Namba, K. Takiyama, and H. Nojima, *Jpn. J.*  
<sup>392</sup> [34] Z. Donkó, P. Hartmann, and K. Kutasi, *Plasma Sources Sci.* <sup>412</sup> *Appl. Phys.* **51**, 066001 (2012).
- <sup>393</sup> *Technol.* **15**, 178 (2006). <sup>413</sup> [45] A. S. Metel, S. N. Grigoriev, Y. A. Melnik, and V. V. Panin,  
<sup>394</sup> [35] G. Fubiani, G. Hagelaar, J. Boeuf, and S. Kolev, *Physics of* <sup>414</sup> *Plasma Phys. Rep.* **35**, 1058 (2009).
- <sup>395</sup> *Plasmas* **19**, 043506 (2012). <sup>415</sup> [46] V. I. Kolobov and A. S. Metel, *J. Phys. D* **48**, 233001 (2015).
- <sup>396</sup> [36] Y. Fu and J. P. Verboncoeur, *IEEE Trans. Plasma Sci.* **47**, 1994 <sup>416</sup> [47] Y. Fu, B. Zheng, D.-Q. Wen, P. Zhang, Q. H. Fan, and J. P.  
<sup>397</sup> (2018). <sup>417</sup> [48] A. Bogaerts, E. Neyts, R. Gijbels, and J. Van der Mullen, *Spectrochim. Acta B* **57**, 609 (2002).
- <sup>398</sup> [37] D. P. Lymberopoulos and D. J. Economou, *J. Phys. D* **28**, 727 <sup>418</sup> [49] A. Wollny, T. Hemke, M. Gebhardt, R. P. Brinkmann, H. Boettner, J. Winter, V. Schulz-von der Gathen, Z. Xiong, M. J. Kushner, and T. Mussenbrock, *Appl. Phys. Lett.* **99**, 141504 (2011).
- <sup>400</sup> [38] M. A. Lieberman and A. J. Lichtenberg, *Principles of Plasma Discharges and Materials Processing* (New York: John Wiley & Sons, 2005). <sup>421</sup> <sup>422</sup> <sup>423</sup> [50] Y. Fu, B. Zheng, D.-Q. Wen, P. Zhang, Q. H. Fan, and J. P. Verboncoeur, *Plasma Sources Sci. Technol.* **29**, 09LT01 (2020).
- <sup>401</sup> <sup>402</sup> [39] Y. Ohtsu and Y. Kawasaki, *J. Appl. Phys.* **113**, 033302 (2013). <sup>424</sup> <sup>425</sup> [40] H. Helm, *Z. Naturforsch. A* **27**, 1812 (1972). <sup>426</sup> <sup>427</sup> [41] J. W. Gewartowski and H. A. Watson, *Principles of Electron Tubes* (Princeton, New Jersey: Van Nostrand, 1965). <sup>428</sup> <sup>429</sup> [42] K. H. Schoenbach, A. El-Habachi, W. Shi, and M. Ciocca, *Plasma Sources Sci. Technol.* **6**, 468 (1997).